On the Role of Physical Processes in Controlling Equatorial Plasma Bubble Morphology

G.A.S. Picanço[1], C.M. Denardini[2], P.A.B. Nogueira[3], P.R. Fagundes[1], A.M. Meza[4], L.P.O. Mendoza[4], M.B. Pádua[2], M.P. Natali[4], L.C.A. Resende[2,5], and L.F.R. Vital[2]

[1] Research and Development Institute, University of Vale of Paraíba (IP&D/UNIVAP), São José dos Campos, Brazil.

[2] National Institute for Space Research (INPE), São José dos Campos, Brazil.

[3] Federal Institute of Education, Science and Technology of São Paulo (IFSP), Jacareí, Brazil.

[4] Faculty of Astronomical and Geophysical Sciences, National University of La Plata (FCAG/UNLP), La Plata, Argentina.

[5] National Space Science Center, Chinese Academy of Sciences (NSSC/CAS), Beijing, China.

Corresponding author: Giorgio Picanço (giorgio.picanco@gmail.com)

Physics and Astronomy Laboratory, Research and Development Institute, University of Vale of Paraíba (IP&D/UNIVAP), Av. Shishima Hifumi, 2911, Urbanova, 12244-010, São José dos Campos, SP, Brazil; Phone: +55 12 3947-1146.

Key Points:

- EPB behavior exhibits a cycle linked with solar flux levels, impacting plasma depletion amplitudes and latitudinal development according to magnetic declination sector.
- During geomagnetically quiet periods, the development of EPBs reveals a saturation point for extreme solar flux values, beyond which the intensification of EPBs ceases to be significant.
- An empirical model is outlined to calculate the maximum latitudinal extent of EPBs based on solar flux and magnetic declination, aiming to provide insights for anticipating EPB behavior across different solar cycle stages and in different longitudinal sectors.

Abstract

In this study, we present the results of an analysis of the morphological features of Equatorial Plasma Bubbles (EPBs) over South America. In this context, we analyzed data from the Disturbance Ionosphere indeX (DIX) maps calculated using around 450 Global Navigation Satellite System (GNSS) stations. To mitigate the influence of magnetic disturbances on bubble development, only data from geomagnetically quiet days were utilized. This study covered the period from the post-peak of solar cycle 24 (2015) to the pre-peak of solar cycle 25 (2023), totaling 1321 nights with EPB occurrences, representing the largest dataset of EPBs ever compiled for South America. Our analysis unveiled several key findings regarding EPBs and

their behavior over the South American region. Firstly, we observed that the amplitude of plasma depletions and the EPB latitudinal development follow an approximately 11-year cycle driven by solar radiation levels. Furthermore, our analysis highlights the significant influence of factors such as vertical plasma drift velocity during the pre-reversal enhancement (PRE), longitudinal variations associated with magnetic declination, as well as the saturation behavior of EPB development with extreme solar flux. Finally, we outline an empirical model to calculate the maximum latitudinal extent of EPBs based on solar flux and magnetic declination as an attempt to provide insights for anticipating EPB behavior across different solar cycle stages and in different longitude sectors.

1 Introduction

Equatorial Plasma Bubbles (EPBs) are ionospheric phenomena characterized by F-region irregularities, where plasma density is significantly reduced when compared with adjacent regions (Kelley, 2009). The process of EPB generation primarily arises from plasma instabilities propagating from lower-density regions (below the F2 layer) to altitudes where the density is higher (the F2 layer) (Haerendel, 1973). The nonlinear evolution of Rayleigh-Taylor Instability (RTI) is the widely accepted primary mechanism for EPB generation in the ionosphere, arising from the upward propagation of this low-density plasma. The RTI initiates through the development of vertical plasma gradients, which result from abrupt enhancements in the nighttime F-region vertical drift velocity. This process often occurs in conjunction with a triggering mechanism at the F-region base, typically linked to atmospheric gravity waves and Large-Scale Wave Structures (LSWS) (Rottger, 1973; Woodman and La Hoz, 1976; Kelley, 2009; Abdu, 1993; Singh et al., 1997a; Taori et al., 2015; Takahashi et al., 2018).

During EPB events, the ionosphere can undergo density differences exceeding two orders of magnitude compared to its initial level. These irregularities diffuse along field lines in both magnetic hemispheres, reaching the highest latitudes as a result of the maximum vertical displacement at the magnetic equator (Abdu et al., 1985; Kelley, 2009; Barros et al., 2018). In this context, EPBs can be studied by analyzing depletions observed in Total Electron Content (TEC) calculated from Global Navigation Satellite Systems (GNSS) data, as they directly impact the ionospheric delay experienced by transionospheric electromagnetic waves (Abdu et al., 1985; Takahashi et al., 2016; Barros et al., 2018). In addition, EPB events can be studied using various other instruments, including Very High Frequency (VHF) radars (Tsunoda, 1985; Abdu et al., 2009), ionosondes (Resende et al., 2019), All-Sky imagers (Pimenta et al., 2003; Paulino et al., 2011; Wrasse et al., 2021), sounding rockets (Abdu et al., 1981; Muralikrishna et al., 2006), and Earth observation satellites (Huang et al., 2012, 2013; McNamara et al., 2013). Hence, the use of different instruments enables the study of these irregularities at different longitudes, latitudes, and altitudes in the ionosphere (Woodman and La Hoz, 1976; Flaherty et al., 1996).

The free electrons in the ionosphere can directly influence the propagation of GNSS signals used in TEC calculation, leading to phase acceleration/delay associated with ionospheric refraction phenomena (Otsuka et al., 2002; Monico, 2008; Takahashi et al., 2016). The analysis of this effect is often employed to estimate the amplitude of TEC variation associated with EPB occurrence, as well as other space weather phenomena (Figueiredo et al., 2018; Wen and Mei, 2020). In this manner, Jakowski et al. (2006) developed the first version of the Disturbance Ionosphere indeX (DIX), which relies on the percentage variation of TEC relative to a given

quiet reference. This study marked the inception of a new trend of innovative ionospheric indices, primarily comprising refined versions of the original one, which were achieved through modifications and the incorporation of new terms into the original equation (Jakowski et al., 2012a, 2012b, 2019; Wilken et al., 2018; Picanço, 2019; Denardini et al., 2020a; Picanço et al., 2020; Barbosa-Neto et al., 2022). Consequently, the DIX provides a quantifiable measure of the ionospheric disturbance level, determined by the variation in TEC associated with ionospheric phenomena driven by external (e.g., geomagnetic storms) (Denardini et al., 2020a; Picanço et al., 2021) and internal (e.g., EPBs) (Denardini et al., 2020b; Picanço et al., 2022) sources.

This study employs a new methodology to investigate ionospheric variability during EPB events, based on the DIX methodology as presented in Picanço (2019) and further developed by Denardini et al. (2020a) and Barbosa-Neto et al. (2020). We initially conducted a comprehensive identification of EPB-related ionospheric disturbances using GNSS data from approximately 450 stations spanning from the post-peak phase of solar cycle 24 to the pre-peak phase of solar cycle 25 (January 2015 to April 2023). This analysis focused on the geomagnetically quiet days between September and April of each year, the peak period of EPB occurrence over the South American region (Barros et al., 2018). Specifically, we focused on the nighttime period, totaling 1321 nights with EPB occurrences, which represents the largest dataset of EPBs ever compiled for South America using GNSS data. The analysis went beyond merely describing the morphology of ionospheric disturbances under different solar activity conditions; it also explored potential physical connections between EPB signatures and the underlying mechanisms governing their key morphological characteristics, including latitudinal extent, estimated length, and depletion amplitude. Furthermore, the analysis covered different sectors of magnetic inclination and declination, seasonal variations, and radiation levels throughout the solar cycle.

The results of this study have unveiled several key findings regarding EPBs and their behavior over the South American region. Firstly, we observed that the amplitude of plasma depletions and the EPB latitudinal development follow an approximately 11-year cycle driven by solar radiation levels. During periods of low solar activity, the EPB cycle commences, with bubble edges closer to the magnetic equator and smaller plasma depletion amplitudes. As solar activity intensifies, EPB edges move away from the magnetic equator, reaching maximum latitudes, and the amplitude of plasma depletion increases. Subsequently, as solar activity diminishes, EPB edges return to near the magnetic equator, reaching a minimum observed latitude, and plasma depletions decrease in magnitude. Additionally, our analysis highlights the significant influence of factors such as vertical plasma drift velocity during the pre-reversal enhancement (PRE), longitudinal variations associated with magnetic declination, as well as the saturation behavior of EPB development with extreme solar flux. Lastly, we outline an empirical model to calculate the maximum latitudinal extent of EPBs based on solar flux and magnetic declination as an attempt to provide insights for anticipating EPB behavior across different solar cycle stages and in different longitude sectors.

2 Methodology

2.1 DIX calculation

In this study we utilized the latest DIX methodology, which combines approaches presented in Picanço (2019), Denardini et al. (2020a), and Barbosa-Neto et al. (2022). We used

the DIX to analyze EPB-related ionospheric disturbances over South America from January 2015 to April 2023, covering the post-peak phase of solar cycle 24 to the pre-peak phase of solar cycle 25. It is worth mentioning that days marked by geomagnetic disturbances, wherein the daily sum of the Kp index exceeds 24, have not been considered in our analysis. Hence, this study investigates EPB events that occur during geomagnetically quiet periods, marking it as the first of its kind to employ the DIX index for climatological purposes. Therefore, an in-depth analysis of ionospheric disturbances related to EPBs is undertaken, with emphasis on their seasonal, latitudinal, longitudinal, and solar activity-induced variations.

The DIX is calculated using Equation (1) as follows (Picanço, 2019; Denardini et al., 2020a; Barbosa-Neto et al., 2022):

$$DIX_k(t) = \left| \frac{\alpha_k\left(\Delta TEC_k(t)/TEC_k^{Qd}(t)\right) + \Delta TEC_k(t)}{\beta} \right|, \quad (1)$$

where $\Delta TEC_k(t) = TEC_k(t) - TEC_k^{Qd}(t)$ is the difference between the measured vertical TEC and the non-perturbed reference, both at a given Ionospheric Pierce-Point (IPP), k. Thus, the term $TEC_k(t)$ represents the vertical TEC calculated for each IPP at a particular time, t. The term $TEC_k^{Qd}(t)$ represents the non-perturbed reference value for the same IPP and time. The value of $TEC_k^{Qd}(t)$ is determined from the 3-hour TEC moving average obtained during the most geomagnetically quiet day within a 15-day window centered on the analyzed day, as described by Picanço et al. (2020). The term α_k represents the $TEC_k^{Qd}(t)$ for $t = 0$ (local midnight), defined considering the IPP geographic longitude. Finally, the term β corresponds to a coefficient dependent on magnetic latitude, which is used to normalize the DIX value on a scale ranging from 0 to greater than 5, as determined by the study of maximum ionospheric disturbances observed during space weather events of solar cycle 24. The values of coefficient β are pre-determined and can be obtained from Barbosa-Neto et al. (2022).

In Table 1, we present a classification of the ionospheric states according to the DIX scale range (Picanço, 2019; Denardini et al., 2020a).

Table 1 - Classification of ionospheric disturbance states based on the DIX scale.

DIX scale ranges	Ionospheric states
[0 - 1]	Quiet
[1 - 2]	Weakly disturbed
[2 - 4]	Disturbed
[4 - 5]	Exceptionally disturbed
> 5	Extremely disturbed

Given the above context, it is noteworthy that the DIX methodology provides an independent value for each individual satellite and time epoch, directly linked to the intensity of ionospheric disturbance measured at the IPP position. The magnitude of the ionospheric disturbance recorded in the DIX varies according to the amplitude of changes in TEC relative to the non-perturbed reference. This magnitude can be higher, as in the case of intense geomagnetic storm events, or lower, as is the case with EPBs. Thus, it is important to highlight that the DIX is a sensitive index that simultaneously responds to various space weather phenomena (Denardini et al., 2020b). While the DIX sensitivity can be advantageous for space weather monitoring, it is crucial to select geomagnetically quiet periods during nighttime hours to ensure that we are studying EPB events with minimal influence from other phenomena.

2.2 Dataset

We used data from an average of 450 GNSS stations distributed throughout Latin America to calculate the DIX for the studied period. These data are freely accessible and originate from several observation networks including the Brazilian Continuous Monitoring Network (RBMC, Brazil), University NAVSTAR Consortium (UNAVCO/EarthScope, USA), National Aeronautics and Space Administration (NASA, USA), Federal Agency for Cartography and Geodesy (BKG, Germany), Argentine Continuous Satellite Monitoring Network (RAMSAC, Argentina), Military Geographic Service (SGM, Uruguay), International GNSS Service (IGS, International), and Low-Latitude Ionospheric Sensor Network (LISN, Peru).

The GNSS observables obtained from the available stations were used calculate multi-constellation and multi-frequency TEC values, following the methodology presented in Mendoza et al. (2019a, 2019b). Subsequently, the obtained TEC data were used to calculate the DIX index for each station individually. Therefore, this work utilized DIX index data calculated using the entirety of available stations, with a sampling rate of 15 seconds. These calculations were based on four GNSS satellite constellations: GPS, GLONASS, Galileo, and BeiDou, according to the available data for each period.

Figure 1 shows the geographical locations of the GNSS stations used in this study. The stations are categorized based on the compatibility of the GNSS receivers with the following constellations: GPS (G: blue circles), GPS and GLONASS (GR: red circles), GPS, GLONASS, and Galileo (EGR: green circles), and GPS, GLONASS, Galileo, and BeiDou (yellow circles).

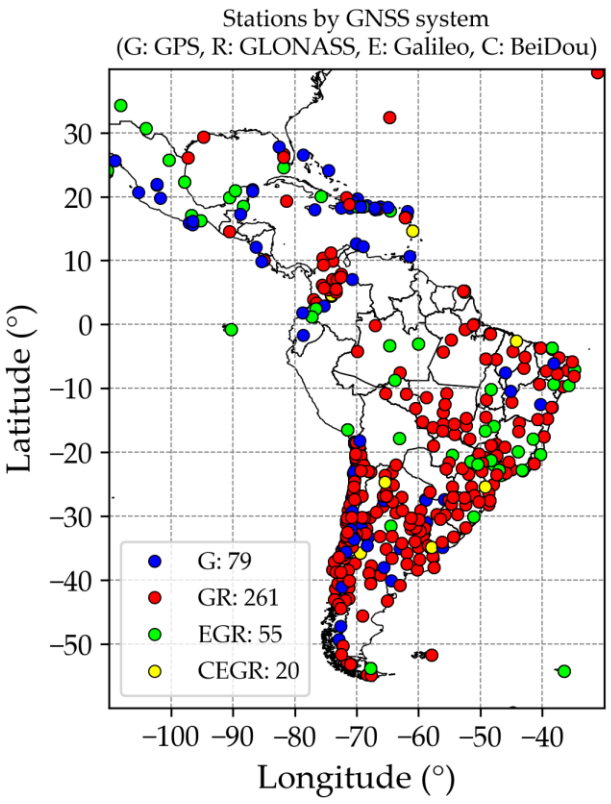

Figure 1: Geographical locations of the GNSS stations used in the study. Blue circles represent stations compatible with GPS, red circles represent stations compatible with GPS and GLONASS, green circles represent stations compatible with GPS, GLONASS, and Galileo, and yellow circles represent stations compatible with GPS, GLONASS, Galileo, and BeiDou.

2.3 Automatic detection and parameterization of EPB-related ionospheric disturbances

After calculating the DIX index for all available stations, we generated interpolated observation matrices over a specific region, referred to as DIXMAPs (Denardini et al., 2020a). This method facilitates the analysis of spatiotemporal variability in the ionosphere and is essential for subsequent stages of the methodology employed in this study, aimed at analyzing the morphological characteristics of EPBs. To generate the DIXMAPs, we utilized the technique described in Takahashi et al. (2016) to interpolate the DIX data obtained from each available GNSS station, assuming a spatial scale of 0.5 degrees. Furthermore, each interpolated matrix incorporates 10 minutes of accumulated DIX data to address observation gaps and mitigate data failures. The generation of DIXMAPs followed the methodology outlined by Denardini et al. (2020a) and Barbosa-Neto et al. (2022).

Following the DIXMAP derivation, we proceeded to analyze the latitudinal, longitudinal, and temporal variability of ionospheric disturbances associated with EPBs over South America by using meridional magnetic cross sections (keograms). These keograms were employed to estimate the morphological parameters of the disturbances by using a new automatic methodology presented in the following lines. Given that EPBs primarily propagate along

geomagnetic field lines, the meridional keograms were constructed based on the coordinates of magnetic meridians. To accomplish this, we divided the DIXMAPs domain into three magnetic meridians: western, central, and eastern, aiming to examine the variability of EPBs within longitudinal sectors and their relationship with magnetic declination angle. This subdivision was done through the calculation of magnetic parameters in the DIXMAP domain using the International Geomagnetic Reference Field model, version 13 (IGRF-13).

Figure 2 illustrates the location of the western (1), central (2), and eastern (3) meridians on January 15, 2015. The red line denotes the geographic coordinates of the magnetic equator on the same date. The colored dots represent the magnetic declination at points along the meridians. It can be observed that the west meridian exhibits low values, the central meridian shows intermediate values, and the east meridian shows high values of magnetic declination within the DIXMAP domain. Additionally, the black dots represent points with magnetic inclination conjugated to the north (+10 degrees magnetic inclination), south (-10 degrees magnetic inclination), and magnetic equator (0 degrees magnetic inclination) along each of the meridians, which will be used as references in the results section.

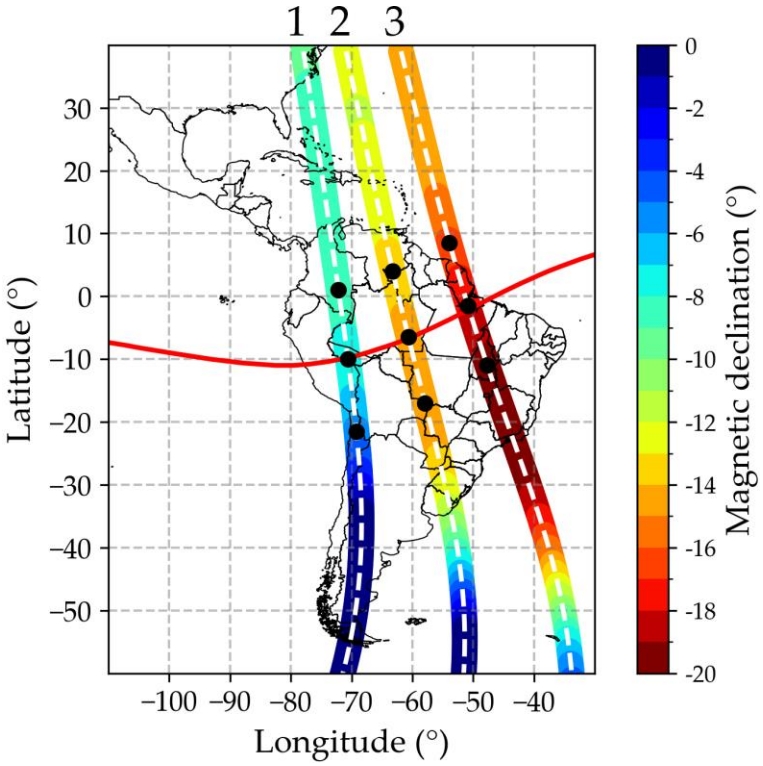

Figure 2: Geographic coordinates of the western (1), central (2), and eastern (3) meridians on January 15, 2015. The red line represents the geographic coordinates of the magnetic equator. The colored symbols represent the values of magnetic declination at each of the meridian points. The black dots represent points with magnetic inclination conjugated to the north (10°), south (-10°), and magnetic equator (0°) along each meridian.

With the aim of facilitating the processing of EPB morphological parameters, we developed a methodology for the automatic identification and parameterization of ionospheric

disturbances related to this phenomenon. The automatic system encompasses the detection of EPB-related ionospheric disturbances using the DIX index, followed by the analysis of their morphological features. For this purpose, the DIX meridional keograms are utilized individually for each night. Any inconsistencies are addressed by cross-referencing the results with data from All-Sky imagers and ionosondes, if necessary, following the validation methodology established by Picanço et al. (2022).

The central approach of this technique involves the binarization of meridional keograms. This is achieved by converting the data into binary matrices, where a value of 1 represents the presence of EPBs and a value of zero indicates their absence. To do this, it is necessary to define a conditional threshold to classify the cells (pixels) of the matrices into binary values. The binary threshold (T) is determined using a technique analogous to a high-pass filter, where the cutoff value is calculated by identifying the most frequent value within the DIX quiet ionosphere scale. The value of T is obtained using Equation (2) below:

$$T = M_o(\mathrm{DIX}), \text{if } DIX(x,y) \leq 1\ , \tag{2}$$

where $M_o(\mathrm{DIX})$ represents the statistical mode (the most frequent value) of the DIX index within the quiet ionosphere scale (between 0 and 1), obtained for each pixel (x, y) of the keogram.

After determining the binary threshold, T, the DIX binary matrix (bin) can be obtained using the relationship presented in Equation (3):

$$bin(x,y) = \begin{cases} 1, & \text{if } DIX(x,y) > T \\ 0, & \text{if } DIX(x,y) \leq T \end{cases} \tag{3}$$

Therefore, keogram cells with values greater than the binary threshold will be defined as one (disturbances), while cells with values less than or equal to the binary threshold will be defined as zero (no disturbances).

After calculating the DIX binary matrix, the methodology proceeds to the disturbance edge detection, aiming to estimate features like the time occurrence intervals and their maximum latitudinal extent. This is achieved by summing the elements of the binary matrix along both the temporal (x-axis) and the latitudinal (y-axis) dimensions.

To determine the maximum latitude extent of disturbances, we perform the sum of columns of the binary matrix, row by row. If the sum results in a value greater than or equal to six time points (where 1 point = 10 min), then the row is classified as 'disturbed'. In this context, we declare an EPB occurrence when the disturbance persists for a minimum duration of 1 hour, following the criteria adopted by Barros et al. (2018). Thus, disturbed rows with values on the y-axis closest to the boundaries of the DIXMAP domain are defined as EPB edges (y_1 and y_2), while other rows are discarded.

The determination of the disturbance time occurrence intervals is performed by summing the rows of the DIX binary matrix, column by column. If the sum results in a value greater than or equal to nine latitude points (where 1 point = 0.5 degrees), then the column is classified as 'disturbed.' We declare an EPB occurrence when the disturbance extends more than 500 km (~4.49 degrees in latitude). Therefore, disturbed columns with values on the x-axis closest to the temporal boundaries of the nighttime keogram (between 18:00 LT and 06:00 LT) are defined as disturbance start and end times (t_1 and t_2), while other columns are discarded.

Both criteria mentioned above are cumulative, and they must be fulfilled to declare the occurrence of an EPB. Additionally, the edges of the EPBs, y_1 and y_2, are compared with the latitude of the magnetic equator on that same magnetic meridian. If there is an asymmetry greater than 30% in the alignment of the EPBs with the magnetic equator, it is deemed insufficient, and the data is marked as 'requiring visual analysis,' where we cross-reference the results with data from All-Sky imagers and ionosondes for further EPB confirmation or rejection.

Figure 3 shows an application example of the developed methodology for the automatic detection and parameterization of EPB-related ionospheric disturbances. Panel 'A' shows the keogram obtained for the central meridian, showing a region of ionospheric disturbance characterized by an intensification in the DIX. In Panel 'B', we show the DIX binary matrix (keogram) obtained through the application of the proposed methodology to the data presented in the meridional keogram (Panel 'A'), with blue lines marking the disturbance edges. The disturbance region (Panel 'C') is then defined by delineating the disturbed rows and columns, where y_1 and y_2 represent the northern and southern edges of the EPB-related disturbances, while t_1 and t_2 represent the disturbance start and end times, respectively. Finally, Panel 'D' illustrates the meridional keogram, marked with the edges of the disturbance region. The dashed black line on the panels represents the geographic latitude of the magnetic equator on the meridian.

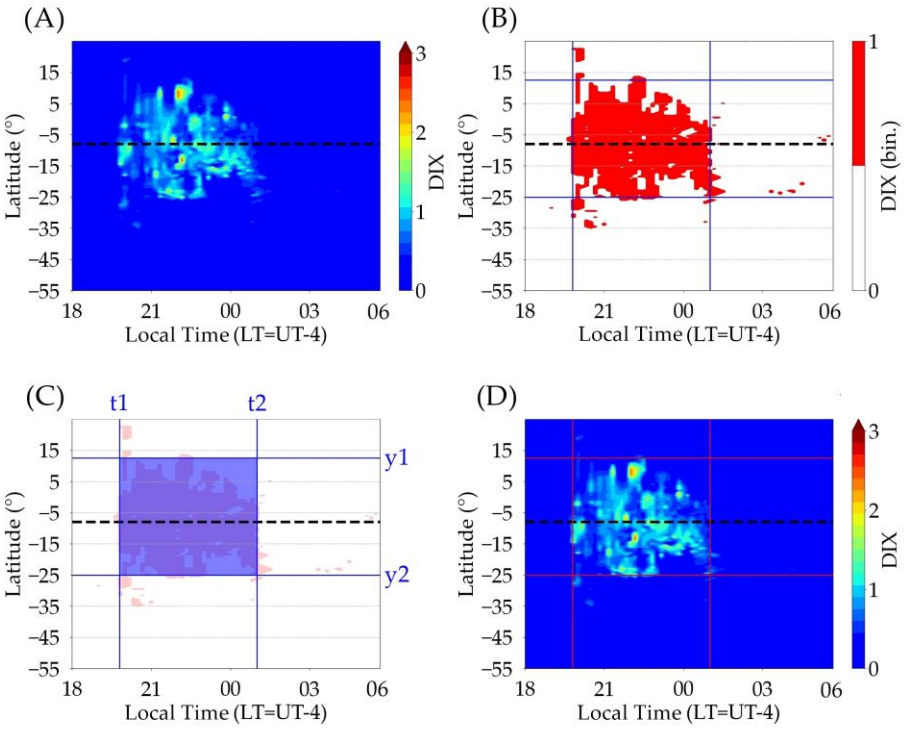

Figure 3 - Example of a meridional DIX keogram (Panel 'A') used to generate the binary keogram (Panel 'B') and identify the edges of EPB-related ionospheric disturbances (blue lines). The coordinates of the disturbed rows and columns used to calculate the occurrence interval (t_1 and t_2) and the latitude extent (y_1 and y_2) of the ionospheric disturbances associated with EPBs are highlighted (Panel 'C'). Additionally, the meridional keogram marked with the disturbance boundaries (red lines, Panel 'D') is shown. The dashed black line represents the geographic latitude of the magnetic equator on the meridian.

2.4 Calculation of EPB latitudinal extent, estimated length, and depletion amplitude

After identifying the edges of the EPB-related ionospheric disturbances, it is possible to obtain their latitudinal extent (LAT), which represents the range of geographic latitudes between y_1 and y_2, as calculated by Equation (4):

$$\mathrm{LAT} = (y_1, y_2) \tag{4}$$

The length of the ionospheric disturbances can be estimated using Equation (5):

$$L = d(y_1 - y_2) \tag{5}$$

where $d = 111.19\,km$ is a conversion factor between degrees (°) and kilometers and represents the corresponding fraction of the Earth's circumference.

At last, the EPB depletion amplitude can be calculated based on the DIX value, as it represents the variation of plasma relative to its nonperturbed reference. The depletion amplitude (A) is calculated as the DIX value at the average time between t_1 and t_2, denoted by $\frac{t_1+t_2}{2}$, given by Equation (6):

$$A = DIX\left(\frac{t_1+t_2}{2}\right) \quad (5)$$

3 Results and Discussion

3.1 Seasonal variation of EPB development over different magnetic declination sectors

In this section, we present results from the analysis of the EPB seasonal behavior regarding their maximum development during geomagnetically quiet periods over different longitude sectors. This analysis utilized data from January 2015 to April 2023 and focused on the geomagnetically quiet days between September and April of each year, which is recognized as the peak period of EPB occurrence over the South American region. Specifically, we focused on the nighttime period, totaling 1321 nights with EPB occurrences, which represents the largest dataset of EPBs ever compiled for South America.

The length of the EPBs, as well as their latitudinal extent, is intrinsically related to the maximum height that the plasma instability reaches at the magnetic equator, since this factor controls the distance that the irregular region diffuses along field lines in both magnetic hemispheres (Whalen, 2002). In this context, the EPB upward displacement over the equatorial region is primarily controlled by the vertical plasma drift velocity during the PRE. According to Barros et al. (2018), more intense vertical drift velocities result in a higher RTI growth, leading to a greater EPB latitudinal development.

In a similar way, some studies suggest that the magnitude of plasma depletion within EPBs can be influenced simultaneously by various factors, including the F-region height and the amount of background plasma, among others (Singh et al., 1997; Wan et al., 2018). Therefore, a better understanding of the seasonal variability and the influence of solar activity on the morphological development of EPBs becomes necessary.

Figure 4 shows the monthly averages of (A) amplitude depletion and estimated length (B) of the EPBs for the western (left panel, in blue), central (middle panel, in red), and eastern (right panel, in green) meridians, covering the months between September and April of the dataset. Additionally, this figure illustrates the monthly averages of (C) the angle calculated between the magnetic meridian and the solar terminator (T-M angle) at 18:00 LT for the three meridians are shown. This analysis follows the discussion presented in Abdu et al. (1992), which suggests that small angles between the solar terminator and the magnetic meridian result in a higher probability of EPBs occurrence.

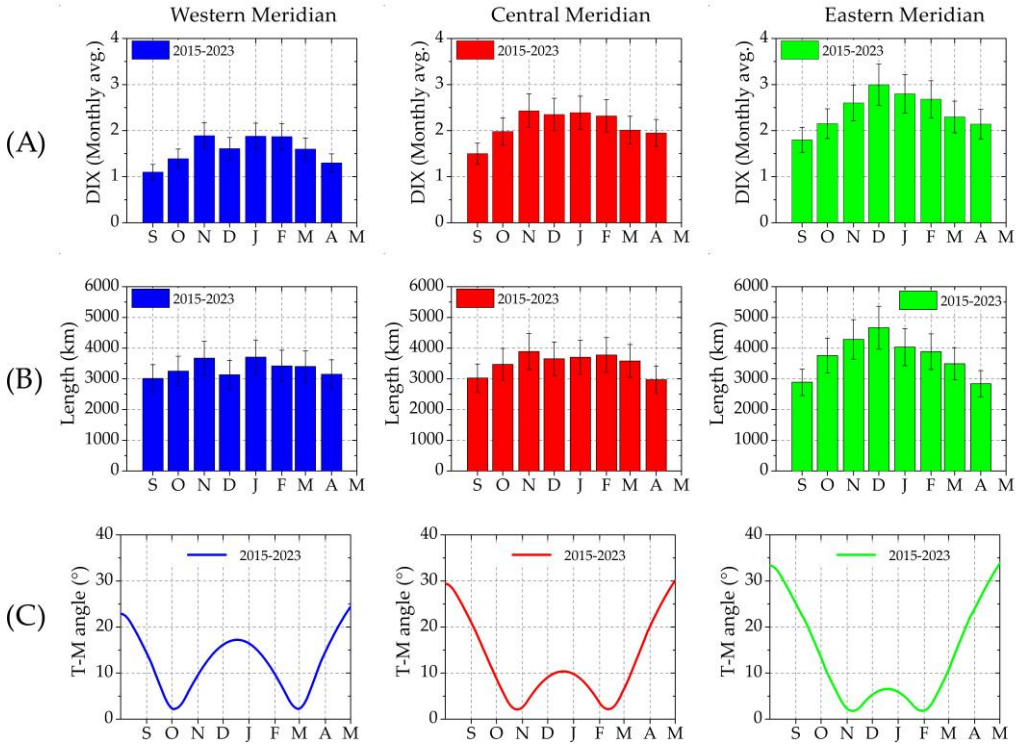

Figure 4: Monthly averages of the (A) EPB amplitude depletion between September and April from the dataset, together with the averages of the (B) EPB length and the (C) T-M angle, for each of the magnetic meridians: western (left column, graphs in blue), central (middle column, graphs in red), and eastern (right column, graphs in green).

The results depicted in Figure 4 confirm a seasonal pattern in the latitudinal and depletion aspects of EPB development during geomagnetically quiet periods. This pattern becomes evident when comparing the monthly averages of amplitude depletion and EPB length (panels A and B) with the T-M angle (panel C). It is observed that the highest lengths and latitudinal extents tend to coincide with periods of lower T-M angles. These periods correspond to months with higher simultaneity between sunset times in conjugated E regions, leading to increased vertical plasma drift velocities, as discussed by Batista et al. (1986). An interesting observation is the more pronounced transition curve between these periods (October and March) in the western meridian, where the T-M angle reaches 18 degrees near December. This results in a noticeable reduction in both the latitudinal development and amplitude depletion of EPBs in this meridian around December. Conversely, the amplitude of the T-M angle during the transition period gradually decreases across the central and eastern meridians. This behavior results in a more consistent development of EPBs during the transition period in these meridians compared to the South American western coast, as observed in the length and depletion panels. Additionally, in the eastern meridian, the T-M angle approaches 5 degrees during the transition period, which is small enough to generate EPBs with the maximum observed development. As emphasized by Abdu et al. (1992), the degree of simultaneity between the magnetic meridian and the solar terminator plays a crucial role in the occurrence frequency of EPBs. The close alignment of the solar terminator with the magnetic meridian results in simultaneous decay of E-region conductivity at both ends of the field line, maximizing the strength of the PRE. Our results

371 further suggest that this aspect also governs the morphological development of these phenomena.
372 Therefore, it is reasonable to expect that a combination of factors, including the magnitude of
373 magnetic declination, contributes to the latitudinal development of EPBs. Thus, it is reasonable
374 to assert that the greater development of EPBs over the eastern South American sector reflects
375 the higher values of vertical plasma drift throughout the year on this meridian, in contrast to the
376 western and central meridians (see Batista et al., 1986; Fejer et al., 2008; Kil et al., 2009).

377

378 3.2 Dependence of EPB amplitude depletion on solar flux and magnetic declination

379 Figure 5 depicts the annual averages of the maximum DIX values during EPB events for
380 each of the magnetic meridians: (A) western, (B) central, and (C) eastern, covering the period
381 from January 2015 to April 2023. In all panels, the annual averages were calculated for each of
382 the three conjugate points (as shown in Figure 2), categorized according to their magnetic
383 inclinations: 10° (symbols in blue), 0° (symbols in red), and -10° (symbols in green).
384 Additionally, the panels include gray bars representing the annual averages of the F10.7 index,
385 expressed in solar flux units (SFU).

386

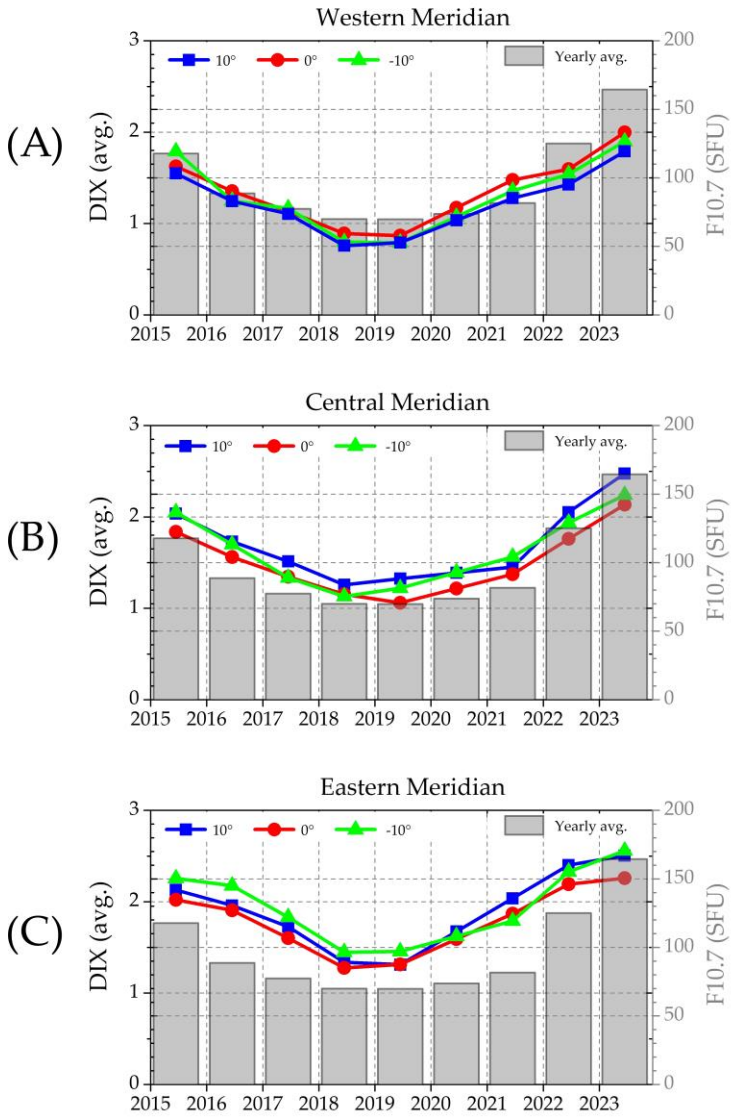

Figure 5: Annual averages of the maximum DIX values calculated during EPB events at conjugate points with magnetic inclinations of 0° (red circles), 10° (blue squares), and -10° (green triangles), obtained in the western (panel 'A'), central (panel 'B'), and eastern (panel 'C') meridians, from 2015 to 2023. The gray bars represent the annual averages of the F10.7 index during the same period.

Based on the results depicted in Figure 5, it is evident that the average curves of maximum DIX intensity during EPBs exhibit a trend similar to the variation of solar activity throughout solar cycles 24 and 25. This similarity is highlighted when comparing the average DIX curves with the annual averages of F10.7 between 2015 and 2019, which span the declining phase and minimum solar activity of solar cycle 24. During this period, there is a decrease of approximately 40.78% in the average solar flux intensity, while the DIX demonstrates a decrease of about 50.46% in the western meridian, 39.21% in the central meridian, and 36.29% in the

eastern meridian. Moving into the rising phase of solar cycle 25 between 2019 and 2023, we observe an increase of approximately 57.60% in the average solar flux intensity. Concurrently, the DIX shows an increase of about 56.92% in the western meridian, 47.43% in the central meridian, and 44.18% in the eastern meridian.

The data reveal significant variability in the rate of intensification and weakening of EPB depletion amplitude in response to changes in solar flux across magnetic meridians in South America. It is noted that the intensity variation of EPBs in relation to solar flux decreases from the west coast towards the central meridian, and subsequently to the eastern meridian. As solar flux increases or decreases, EPBs exhibit distinct trends in each of these regions, highlighting the substantial influence of geographical location and magnetic declination on the rate of intensification or weakening of EPBs in response to solar flux variations.

Another interesting observation is that when comparing panels A, B, and C from Figure 5, the amplitudes of the annual DIX averages tend to be smaller in the western meridian, intermediate in the central meridian, and higher in the eastern meridian. This longitudinal variation correlates with the TEC variation between these sectors, with higher values observed on the eastern coast compared to the western coast of South America (Nogueira et al., 2013). Additionally, these differences can be attributed to the strength of the PRE, which is higher on the eastern coast than on the western coast of South America (Batista et al., 1986). It is noteworthy that both plasma density and the intensity of the PRE exhibit a strong dependence on solar flux (Liu et al., 2009; Fejer et al., 2008).

The results presented in Figure 5 also indicate that magnetic declination plays a significant role in the longitudinal variation of EPB depletion, which agrees with the vertical drift velocity behavior over different declination sectors (Batista et al., 1986). Consequently, the vertical drift velocity during the PRE period tends to increase with magnetic declination and exhibits seasonal variations in its intensity peaks (Tsunoda, 1985). Furthermore, Abdu et al. (1981) noted a similar relationship between EPB occurrence and magnetic declination angle. In summary, our findings suggest that the amplitude of EPB plasma depletions is proportional to the intensity of solar energy input into the ionosphere-thermosphere system, which varies as the solar cycle ascends and descends over an approximately 11-year period (Gnevyshev, 1967).

Figure 6 shows the relationship between the percentage rate of change (%) of the DIX annual averages during EPBs and the F10.7 index for the (A) western, (B) central, and (C) eastern meridians, covering the period from 2015 to 2023. The rate of change was calculated based on the data presented in Figure 5, using the values of 2019 (solar minimum) as a fixed reference. Vertical lines indicate specific stages of the solar flux variation: '1' represents the solar minimum in 2019, '2' represents the post-peak phase of solar cycle 24 in 2015, and '3' represents the pre-peak phase of solar cycle 25 in 2023. The solid black lines represent the exponential function fittings calculated for each magnetic meridian.

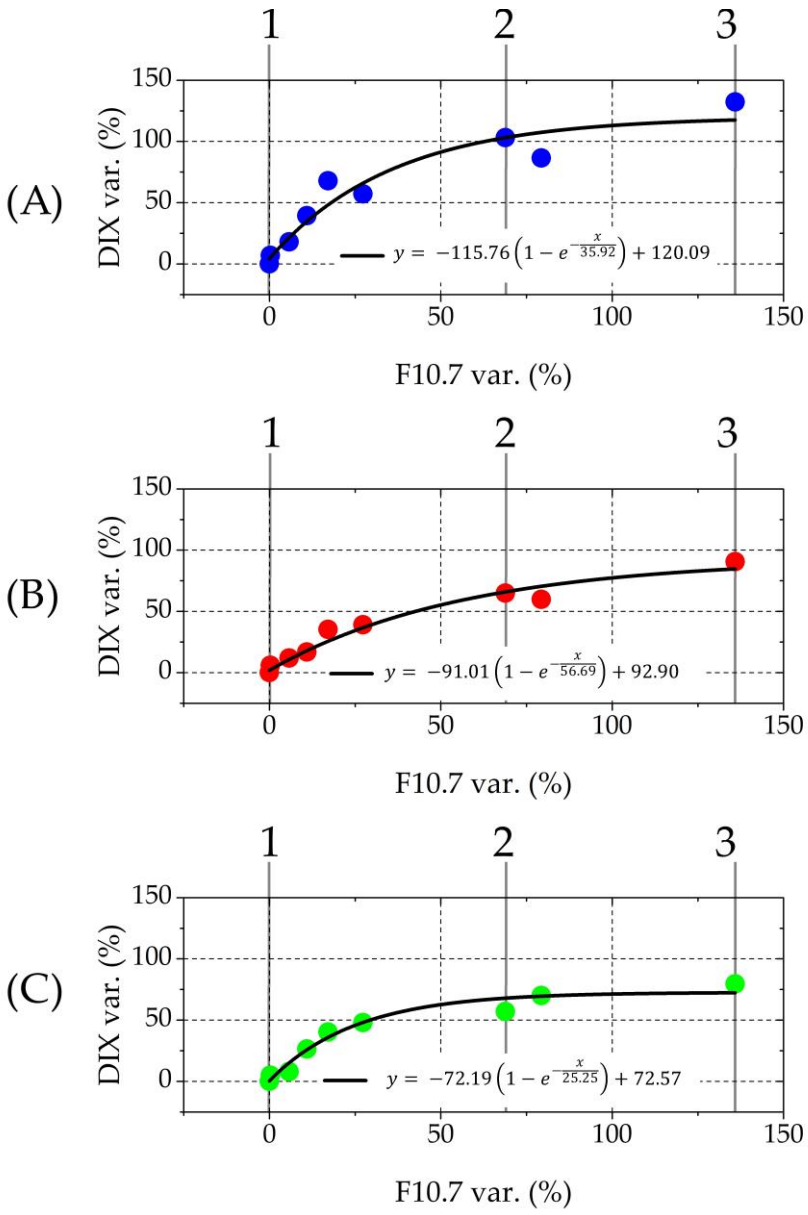

Figure 6: Scatter plots illustrating the relationship between the percentage rate of change in annual averages of the F10.7 index and the DIX during EPBs relative to the solar minimum occurring between solar cycles 24 and 25, for the western (A), central (B), and eastern (C) meridians. Vertical lines indicate specific stages of the solar cycles: '1' represents the solar minimum in 2019, '2' represents the post-peak phase of solar cycle 24 in 2015, and '3' represents the pre-peak phase of solar cycle 25 in 2023.

It is evident that the EPBs depletion amplitude tends to increase with solar activity, as can be seen in Figure 6. However, this relationship is not linear and exhibits saturation at high values of solar flux. Analysis across the different meridians reveals varying patterns. In the (Figure 6A) western meridian, the DIX index increases by approximately 100% (DIX ≈ 1.65) compared to the value observed at solar minimum (DIX ≈ 0.81), with a corresponding intensification of solar

flux by approximately 69.8% (about 117 SFU in 2015). Conversely, in the (Figure 6B) central meridian, the DIX increase approaches 100% (DIX ≈ 2.28) relative to the value observed at solar minimum (DIX ≈ 1.20), accompanied by a more significant intensification of solar flux, approximately 135% (about 164 SFU in 2023). Lastly, in the (Figure 6C) eastern meridian, the DIX increase does not reach 100% compared to the value observed at solar minimum (DIX ≈ 1.36), peaking at a maximum variation rate of 79.52% (DIX ≈ 2.43), with a similar increase of approximately 135% in solar flux (about 164 SFU in 2023).

Upon observing the exponential functions modeled for the western, central, and eastern meridians of South America, distinct responses emerge concerning the DIX variation in relation to solar flux. Analysis of the coefficients of the exponential functions reveals notable differences. The western meridian exhibits a higher rate of EPB intensification, with a coefficient of 115.76, indicating a more immediate response to changes in solar flux. Saturation is reached with a 120.09% increase in F10.7 intensity compared to the value observed at solar minimum, representing the peak intensity of EPBs during the period. Beyond this point, the rate of EPB intensity increase decreases significantly. In contrast, the eastern meridian demonstrates a lower rate of intensification, with a coefficient of 72.19, indicating a more gradual growth. However, EPBs reach saturation more readily over the eastern meridian, occurring with a 72.57% increase in F10.7 intensity compared to the value observed at solar minimum. Additionally, the central meridian presents an intensification rate of 91.01, with an inflection point at 56.09. In this case, saturation occurs with a 92.90% increase in F10.7 observed during solar minimum.

The analysis of the coefficients of the exponential function for each meridian underscores a strong relation between the variation in EPB-related depletion amplitudes and longitudinal sectors. These coefficients offer detailed insights into the distinctive characteristics of each region concerning the variability of solar flux. The functional analysis reveals diverse response patterns of EPBs to solar flux variations across South America meridians. The western meridian, characterized by a rapid initial rate of intensification, demonstrates heightened sensitivity, ultimately reaching saturation. Conversely, the eastern meridian, despite exhibiting a lower initial rate, achieves saturation more expeditiously, indicating earlier stabilization compared to other meridians. Positioned between these extremes, the central meridian shows a notable equilibrium, manifesting an intermediate initial rate and intensification of solar activity leading to saturation. These insights gleaned from the exponential functions elucidate the unique features of each region concerning EPBs, illustrating how distinct meridional sectors respond uniquely to fluctuations in solar flux.

From the results presented in Figure 6, it is evident that the saturation point of the maximum EPB development during geomagnetically quiet periods tends to increase with magnetic declination. This trend may be attributed to the vertical plasma drift velocity during the PRE, which governs the amplitude of plasma depletion observed during EPBs. Previous studies by Fejer et al. (1991) and Santos et al. (2013) have also documented saturation in the intensification of the PRE peak relative to solar flux across the entire South American sector. Consequently, sectors with higher declination require lower solar flux levels to achieve the same maximum vertical drift velocity observed in sectors with lower declination.

3.3 EPB latitudinal development relation with solar flux and magnetic declination

Figure 7 shows the temporal evolution of the maximum latitudinal extent of EPBs from 2015 to 2023 for the western (A), central (B), and eastern (C) meridians. In each panel, the red lines denote the geographic latitude of the magnetic equator for the corresponding meridian. Symbols positioned above the magnetic equator line represent the maximum extent of EPBs in the northern magnetic hemisphere, while those below represent the maximum extent in the southern magnetic hemisphere. Accompanying the symbols are black lines representing the annual averages of the maximum latitudinal extensions in each magnetic hemisphere. Additionally, gray bars depict the (D) annual averages of the F10.7 index during the same period.

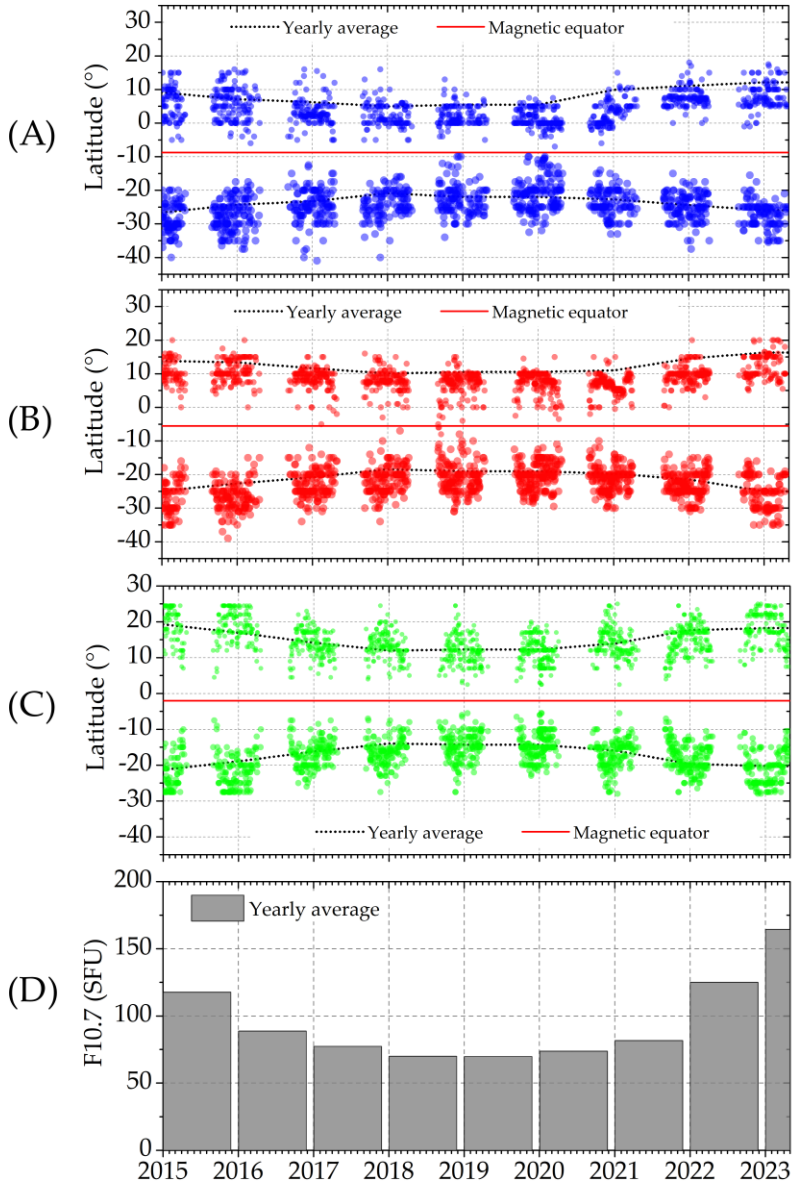

Figure 7: Temporal variation of the maximum latitudinal extensions reached by EPBs in the western (panel A), central (panel B), and eastern (panel C) meridians during the period between January 2015, and April 2023. In all panels, the black lines represent the annual averages of the maximum extensions, while the red lines represent the latitude of the magnetic equator in each of the meridians. The gray bar chart (panel 'D') represents the annual averages of the F10.7 index during the same period.

Figure 7 shows that, like the intensity of the plasma depletions, the EPB latitudinal extent also follows the trend of the solar cycle variation. This can be evidenced in panels A, B, and C through their comparison with the annual average of the F10.7 index (panel D). In summary, it is observed that the edges of the EPBs tend to be displaced from the magnetic equator during periods of high solar activity (2015 and 2023) and closer to the magnetic equator during periods of low solar activity (2019). These results demonstrate that EPBs develop over a cycle of approximately 11 years, which is controlled by the variability of solar activity (Gnevyshev, 1967). In this way, EPBs present lower development in the in the latitudinal and depletion aspects during periods of low solar activity, where their edges are closer to the magnetic equator. Throughout the ascending phase of the solar cycle, the edges of the EPBs tend to move away from the magnetic equator, reaching a maximum possible latitude. Then, in the descending phase of the solar cycle, the EPBs begin to approach the magnetic equator again, reaching a minimum latitude.

Given the direct relationship between the latitudinal extent of EPBs and their maximum height at the magnetic equator (Pimenta et al., 2003; Kelley, 2009), the findings presented in this section align with the mechanisms driving the variability in EPB intensity concerning solar activity, the intensity of the PRE, and magnetic declination. It is evident that the latitudinal extent of EPBs is influenced by solar flux, which fluctuates with the periods of solar activity rise and decline. Nevertheless, it is crucial to highlight the existence of a saturation point in EPB development concerning solar flux, as discussed in Section 3.2. Thus, we anticipate a saturation point in the maximum latitude reached by EPBs.

3.4 Proposal of an empirical model for EPB latitudinal development under different solar flux levels and magnetic declination sectors

In this section, we present the results of a mathematical model concerning the variability in the EPB latitudinal development for different levels of solar flux and magnetic declination sectors. The model was developed empirically using the data presented in Sections 3.1 to 3.3, grounded on theoretical foundations from key studies in the scientific literature on EPB development.

Figure 8 presents the relationship between EPB length (km) and solar flux (SFU), considering the data obtained between 2015 and 2023. Each scatter plot includes black lines representing logarithmic function fits made to each dataset. Blue plots denote data from the western meridian, red plots represent data from the central meridian, and green plots correspond to data from the

eastern meridian. The fit equation for these scatter plots is presented and discussed in the following lines.

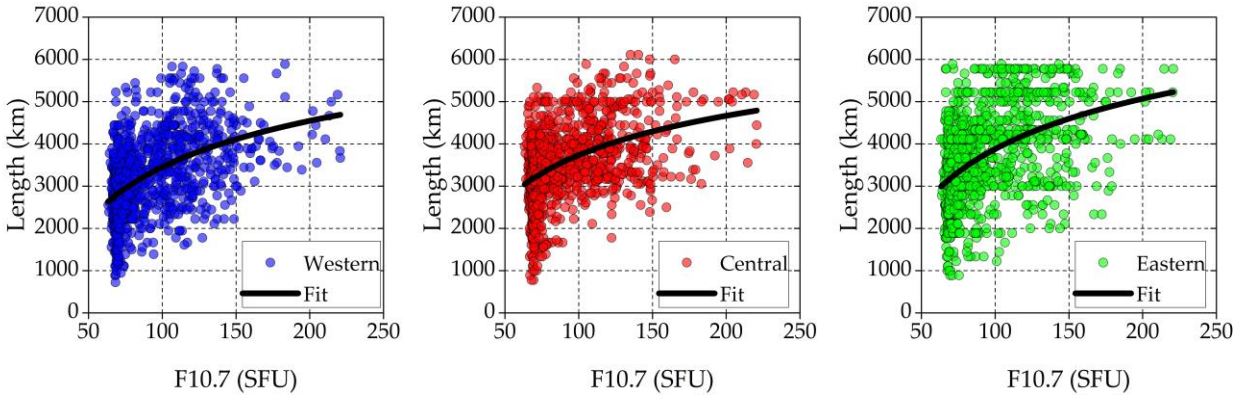

Figure 8: Scatter plots representing the relationship between F10.7 values (SFU) and the lengths (km) of EPBs from January 2015 to Abril 2023 for the western meridian (left panel, in blue), central meridian (center panel, in red), and eastern meridian (right panel, in green). The black lines represent the logarithmic function fits made for each meridian.

Figure 8 highlights important EPB morphological characteristics. We observe that the length increases in response to the intensification of solar flux. However, there is an evident saturation tendency in EPB development for high solar flux values. These results agree with previous studies, which consider the variability of various equatorial ionospheric electrodynamics phenomena as a function of solar activity (Fejer et al., 1991; Nogueira et al., 2013; Santos et al., 2013). In this sense, we emphasize that this saturation point is related to the physical limits associated with the main EPB generation mechanisms during geomagnetically quiet periods, such as PRE, thermospheric wind, and Pedersen conductivity near sunset.

Analyzing the results presented in Figure 8, we note that the relationship between the latitudinal development of EPBs and solar flux is indeed nonlinear. Another notable morphological aspect is the significant variation in EPB length among meridians. Specifically, EPBs exhibit greater lengths in the eastern meridian, followed by the central meridian, while showing smaller values in the western meridian. This leads to the following observations:

- During the peak of the solar cycle, EPBs reach their maximum development.
- This development is directly associated with the intensification of irregularity-generating mechanisms.
- The relationship between the intensification of solar flux and EPB development follows an increasing, yet nonlinear trend, exhibiting saturation after a certain level of solar flux.
- Longitudinal variation in EPB length is observed, which correlates with the magnitude of the magnetic declination angle.

The use of logarithmic fits depicted in Figure 8 enabled us to mathematically model the latitudinal development of EPBs concerning solar flux and magnetic declination. Thus, we employed the fit equation to establish an empirical model for estimating the maximum length (L_{max}) of EPBs based on solar activity and magnetic declination. Equation 6 presents the mathematical expression of the L_{max} model, denoted in kilometers:

$$L_{max} = 1{,}375a * \ln(-b * \ln(SF)) \,, \tag{6}$$

where a and b are the scale and vertical translation coefficients of the logarithmic function, individually obtained for each fit presented in Figure 8. SF represents the F10.7 index, given in solar flux units (SFU).

Below, we demonstrate a method to derive these coefficients as functions of the magnetic declination of each meridian, simplifying the calculation process.

Figure 9 shows scatter plots of the coefficients a (left panel) and b (right panel) obtained for each of the three meridians, showing their variation with the magnetic declination of each one. The blue symbols, from left to right, represent the meridians from west to east. The red lines depict the linear fits obtained for each dataset.

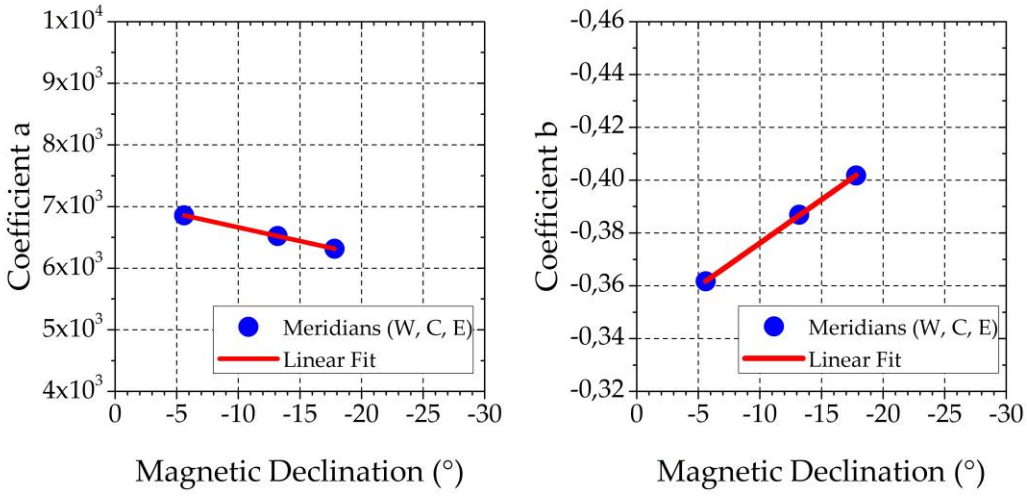

Figure 9: Scatter plots depicting the linear relationship between the values of coefficients a (left panel) and b (right panel) and the magnetic declination of each meridian. The red line in each panel represents the linear fit of the obtained function.

606

607

608 The equations for fitting the coefficients a and b are given by:

$$a = 7{,}1046 \times 10^{3} + (44{,}28(D)) \quad (7)$$

609

$$b = -3{,}4 \times 10^{-1} + (3{,}3 \times 10^{-3}(D)) \quad (8)$$

610

611 where D represents the modulus of the magnetic declination at the magnetic equator latitude.

612

613 The equation for L_{max} can also estimate the maximum EPB latitudinal extent in both
614 North and South magnetic hemispheres. This can be done using the following equations:

615

$$y_1 = \frac{1}{2}\left(\frac{L_{max}}{d}\right) + \phi_{eq} \quad (9)$$

616

617

$$y_2 = -\frac{1}{2}\left(\frac{L_{max}}{d}\right) - \phi_{eq} \quad (10)$$

618

619 where $d = 111.19\ km$ is the conversion factor between kilometers and degrees (°), and ϕ_{eq} is
620 the latitude of the magnetic equator.

621

622 **4 Summary and Conclusions**

623 In this work we have investigated the morphological characteristics of EPBs and their
624 relationship with the variability of their generation physical mechanisms. Accordingly, a
625 methodology based on GNSS data was developed to quantify the variability of ionospheric
626 plasma during the occurrence of ionospheric disturbances associated with EPBs. This
627 methodology was applied to study the characteristics of EPBs throughout different stages of
628 solar cycles 24 and 25, considering various physical aspects of the study area. Therefore, the
629 results were analyzed with a focus on understanding the nighttime ionospheric electrodynamics
630 during geomagnetically quiet periods between 2015 and 2023, corresponding to the interval
631 between the post-peak phase of solar cycle 24 and the pre-peak phase of solar cycle 25. The main
632 conclusions obtained from this work are summarized as following:

633 1. The amplitude of depletion and the latitudinal development of plasma bubbles follow
634 an approximately 11-year cycle, dictated by solar activity levels. This cycle begins

during periods of low solar activity when the edges of these bubbles are closer to the magnetic equator, and the amplitude of plasma depletions is smaller. As solar activity increases, the edges of EPBs move farther from the magnetic equator, reaching their maximum latitudinal extent, while the amplitude of plasma depletions grows. Subsequently, during periods of decreasing solar activity, the edges of EPBs return closer to the magnetic equator, reaching a minimum observed latitude, accompanied by a reduction in the magnitude of plasma depletions.

2. The latitudinal extent of EPBs exhibits longitudinal variations associated with magnetic declination. This factor is related to the degree of simultaneity between the magnetic meridian and the solar terminator (T-M angle), which controls the time difference between sunset times at conjugate points in Region E. Therefore, the smaller the T-M angle, the higher the vertical plasma drift velocity during the occurrence of PRE, resulting in EPBs with greater latitudinal extent.

3. The seasonal variability of EPB intensity shows a dependence on longitudinal sector. In this context, more intense plasma depletions are observed over the west coast of South America during the equinox months. On the other hand, on the east coast, the peaks of EPB intensity exhibit a similar pattern in both equinox and summer months.

4. An explanation for the seasonal behavior in EPB intensity is related to differences between the west and east coasts of South America, both in terms of the amount of plasma in the environment and the intensity of the PRE. On the west coast, TEC and PRE values reach higher levels during the equinox months, leading to more intense disturbances in DIX during these periods. On the other hand, on the east coast, the highest TEC values are observed in the equinox months, while the peaks of PRE occur during the summer. This configuration results in a less evident semi-annual variation in EPB intensity along the east coast. As a result, intensity peaks in DIX occur closer to December in this region, although elevated values are still observed during the summer months.

5. The latitudinal development and amplitude of plasma depletion in EPBs increase as solar flux intensifies. However, a saturation behavior is observed in this dependence, which is related to the physical limits associated with the main formation mechanisms of EPBs during geomagnetically quiet periods, such as PRE, thermospheric wind, and Pedersen conductivity near sunset.

6. An empirical model was developed to calculate the maximum latitudinal extent of EPBs as a function of solar flux and magnetic declination. This model provides important information that can be used to estimate EPB development during different stages of the solar cycle and in different longitudinal sectors.

Acknowledgments

The authors would like to express their gratitude to the following networks and organizations for providing the GNSS data essential for this study: RBMC, RAMSAC, LISN, UNAVCO, NASA, BKG, SGM, and IGS. Special thanks to NASA/OMNIWeb for supplying the F10.7 data, and to IAGA/NOAA for providing the IGRF-13 model. Additionally, we acknowledge GFZ Potsdam for the Kp index. G. A. S. Picanço extends sincere thanks to the São Paulo Research Foundation (FAPESP) for financial support through grant 2023/07518-7, and to

Capes/MEC (grants 88887.467444/2019-00 and 88887.685060/2022-00). We are also grateful to Barros, D. S., and Wrasse, C. M. for providing the interpolation program utilized in this study. Finally, we would like to thank the Brazilian Ministry of Science, Technology, and Innovation (MCTI) and the Brazilian Space Agency (AEB) for their support.

Data Availability Statement

GNSS data from the networks and organizations mentioned, including RBMC (https://geoftp.ibge.gov.br), RAMSAC (https://www.ign.gob.ar), LISN (http://lisn.igp.gob.pe/jdata), UNAVCO (https://data.unavco.org), NASA (https://cddis.nasa.gov), BKG (https://igs.bkg.bund.de), SGM (http://www.igm.gub.uy), and IGS (https://igs.org), can be accessed through the respective databases of each institution upon prior registration. The F10.7 data is available on the NASA/OMNIWeb website (https://omniweb.gsfc.nasa.gov). The IGRF-13 Python version model can be found on the project page (https://pypi.org/project/pyIGRF). Additionally, the Kp index can be accessed on the GFZ website.

References

Abadi, P., Otsuka, Y., & Tsugawa, T. (2015). Effects of pre-reversal enhancement of E × B drift on the latitudinal extension of plasma bubble in Southeast Asia. Earth, Planets and Space, 67, e74. https://doi.org/10.1186/s40623-015-0246-7.

Abdu, M. A., Bittencourt, J. A., & Batista, I. S. (1981). Magnetic declination control of the equatorial F region dynamo field development and spread F. Journal of Geophysical Research: Space Physics, 86(11), 11443–11446. https://doi.org/10.1029/JA086iA13p114403

Abdu, M. A., Sobral, J. H. A., Nelson, O. R., & Batista, I. S. (1985). Solar cycle related range type spread-F occurrence characteristics over equatorial and low latitude stations in Brazil. Journal of Atmospheric and Terrestrial Physics, 47(8–10), 901-905. https://doi.org/10.1016/0021-9169(85)90065-0

Abdu, M. A., Batista, I. S., & Sobral, J. H. A. (1992). A new aspect of magnetic declination control of equatorial spread F and F region dynamo. Journal of Geophysical Research, 97(A10), e14897. https://doi.org/10.1029/92ja00826

Abdu, M. A. (1993). Equatorial spread F and ionosphere–thermosphere system: a review. Trends in Geophysics Research, 2, 193-209.

Abdu, M. A., Batista, I. S., Reinisch, B. W., Souza, J. R., Sobral, J. H. A., Pedersen, T. R., ... Groves, K. M. (2009). Conjugate Point Equatorial Experiment (COPEX) campaign in Brazil: electrodynamics highlights on spread F development conditions and day-to-day variability. Journal of Geophysical Research, 114(A04308). https://doi.org/10.1029/2008JA013749

Barbosa-Neto, P. F., Picanço, G. A. S., De Nardin, C. M., Nogueira, P. A. B., Resende, L. C. A., & Moro, J. (2022). Evaluation of the DIX scaling factor during geomagnetically disturbed periods over South America. Brazilian Journal of Geophysics, 40(4), 1-17.

https://doi.org/10.22564/brjg.v40i4.2191

Barros, D., Takahashi, H., Wrasse, C. M., & Figueiredo, C. A. O. B. (2018). Characteristics of equatorial plasma bubbles observed by TEC map based on groundbased GNSS receivers over South America. Annales Geophysicae, 36, 91–100. https://doi.org/10.5194/angeo-36-91-2018

Batista, I. S., Abdu, M. A., & Bittencourt, J. A. (1986). Equatorial F region vertical plasma drifts: seasonal and longitudinal asymmetries in the American sector. Journal of Geophysical Research: Space Physics, 91(A11), 12,055–12,064. https://doi.org/10.1029/JA091iA11p12055

Denardini, C. M., Picanço, G. A. S., Barbosa-Neto, P. F., Nogueira, P. A. B., Carmo, C. S., Resende, L. C. A., ... Bilibio, A. V. (2020a). Ionospheric scale index map based on TEC data for space weather studies and applications. Space Weather, 18, e2019SW002328. https://doi.org/10.1029/2019SW002328

Denardini, C. M., Picanço, G. A. S., Barbosa-Neto, P. F., Nogueira, P. A. B., Carmo, C. S., Resende, L. C. A., ... Bilibio, A.V. (2020b). Ionospheric scale index map based on TEC data during the Saint Patrick magnetic storm and EPBs. Space Weather. https://doi.org/10.1029/2019sw002330

Fejer, B. G., Gonzalez, S. A., & Woodman, R. F. (1991). Average vertical and zonal F-region plasma drifts over Jicamarca. Journal of Geophysical Research: Space Physics, 96(A8), 13,901–13,906. https://doi.org/10.1029/91JA01171

Fejer, B. G., Jensen, J. W., & Su, S. Y. (2008). Seasonal and longitudinal dependence of equatorial disturbance vertical plasma drifts. Geophysical Research Letters, 35, L20106. https://doi.org/10.1029/2008GL035584

Flaherty, J. P., Kelley, M. C., Seyler, C. E., & Fitzgerald, T. J. (1996). Simultaneous VHF and transequatorial HF observations in the presence of bottomside equatorial spread F. Journal of Geophysical Research: Space Physics, 101(A12), 26811–26818. https://doi.org/10.1029/96JA01115

Figueiredo, C. A. O. B., Takahashi, H., Wrasse, C. M., Otsuka, Y., Shiokawa, K., & Barros, D. (2018). Medium-scale traveling ionospheric disturbances observed by detrended total electron content maps over Brazil. Journal of Geophysical Research: Space Physics, 123, 2215–2227. https://doi.org/10.1002/2017JA025021

Gnevyshev, M. N. (1977). Essential features of the 11-year solar cycle. Solar Physics, 51, 175–183. https://doi.org/10.1007/BF00240455

Haerendel, G., Eccles, J. V., & Cakir, S. (1992). Theory of modeling the equatorial evening ionosphere and origin of the shear in horizontal plasma flow. Journal of Geophysical Research, 97(A2), 1209–1223.

Huang, C. S., La Beaujardiere, O., Roddy, P. A., Hunton, D. E., Ballenthin, J. O., & Hairston, M. R. (2012). Generation and characteristics of equatorial plasma bubbles detected by the C/NOFS satellite near the sunset terminator. Journal of Geophysical Research, 117(A11). https://doi.org/10.1029/2012ja018163

Huang, C. S., La Beaujardière, O., Roddy, P. A., Hunton, D. E., Ballenthin, J. O., Hairston, M.

R., & Pfaff, R. F. (2013). Large-scale quasiperiodic plasma bubbles: C/NOFS observations and causal mechanism. Journal of Geophysical Research, 118(6), 3602–3612. https://doi.org/10.1002/jgra.50338

Jakowski, N., Stankov, S. M., Schlueter, S., & Klaehn, D. (2006). On developing a new ionospheric perturbation index for space weather operations. Advances in Space Research, 38(11), 2596–2600. https://doi.org/10.1016/j.asr.2005.07.043

Jakowski, N., Borries, C., & Wilken, V. (2012a). Introducing a disturbance ionosphere index. Radio Science, 47(4). https://doi.org/10.1029/2011rs004939

Jakowski, N., Béniguel, Y., De Franceschi, G., Pajares, M. H., Jacobsen, K. S., Stanislawska, I., Tomasik, L., Warnant, R., & Wautelet, G. (2012b). Monitoring, tracking and forecasting ionospheric perturbations using GNSS techniques. Journal of Space Weather and Space Climate, 2. https://doi.org/10.1051/swsc/2012022

Jakowski, N., & Hoque, M. M. (2019). Estimation of spatial gradients and temporal variations of the total electron content using ground-based GNSS measurements. Space Weather, 17, 339–356. https://doi.org/10.1029/2018SW002119

Kelley, M. C. (2009). The Earth's ionosphere: Plasma physics and electrodynamics (2nd ed.). Academic Press.

Kil, H., Oh, S. J., Paxton, L. J., & Fang, T. W. (2004). High-resolution vertical ExB drift model derived from ROCSAT-1 data. Journal of Geophysical Research, 114, A10314. https://doi.org/10.1029/2009JA014324

Liu, L., Zhao, B., Wan, W., Ning, B., Zhang, M. L., & He, M. (2009). Seasonal variations of the ionospheric electron densities retrieved from Constellation Observing System for Meteorology, Ionosphere, and Climate mission radio occultation measurements. Journal of Geophysical Research, 114, A02302. https://doi.org/10.1029/2008JA013819

McNamara, L. F., Caton, R. G., Parris, R. T., Pedersen, T. R., Thompson, D. C., Wiens, K. C., & Groves, K. M. (2013). Signatures of equatorial plasma bubbles in VHF satellite scintillations and equatorial ionograms. Radio Science, 48(2), 89–101. https://doi.org/10.1002/rds.20025

Mendoza, L. P. O., Meza, A. M., & Aragón Paz, J. M. (2019a). A multi-GNSS, multi-frequency and near real-time ionospheric TEC monitoring system for South America. Space Weather. https://doi.org/10.1029/2019sw002187

Mendoza, L. P. O., Meza, A. M., & Aragón Paz, J. M. (2019b). Technical note on the multi-GNSS, multi-frequency and near real-time ionospheric TEC monitoring system for South America. EarthArXiv. https://doi.org/10.31223/osf.io/3vts6

Muralikrishna, P., & Abdu, M. A. (2006). Rocket measurements of ionospheric electron density from Brazil in the last two decades. Advances in Space Research, 37(5), 1091–1096. https://doi.org/10.1016/j.asr.2006.02.006

Monico, J. F. G. (2008). GNSS Positioning: Description, Fundamentals, and Applications (2nd ed.). UNESP.

National Oceanic and Atmospheric Administration (NOAA). (2023). Solar cycle progression. Retrieved from https://www.swpc.noaa.gov/products/solar-cycle-progression. Accessed

August 21, 2023.

Nogueira, P. A. B., Abdu, M. A., Souza, J. R., Bailey, G. J., Batista, I. S., Shume, E. B., & Denardini, C. M. (2013). Longitudinal variation in Global Navigation Satellite Systems TEC and topside ion density over South American sector associated with the four-peaked wave structures. Journal of Geophysical Research: Space Physics, 118(12), 7940–7953. https://doi.org/10.1002/2013ja019266

Otsuka, Y., Ogawa, T., Saito, A., et al. (2002). A new technique for mapping of total electron content using GPS network in Japan. Earth, Planets and Space, 54, 63–70.

Paulino, I., Medeiros, A. F., Buriti, R. A., Takahashi, H., Sobral, J. H. A., & Gobbi, D. (2011). Plasma bubble zonal drift characteristics observed by airglow images over Brazilian tropical region. Brazilian Journal of Geophysics, 29(2), 239–246. https://doi.org/10.1590/S0102-261X2011000200003

Picanço, G. A. S. (2019). Development and analysis of an ionospheric index based on Total Electron Content data (Master's thesis, Space Geophysics/Solar-Terrestrial Environmental Sciences). National Institute for Space Research.

Picanço, G. A. S., Denardini, C. M., Nogueira, P. A. B., Barbosa-Neto, P. F., Resende, L. C. A., Carmo, C. S., Romero-Hernandez, E., Chen, S. S., Moro, J., & Silva, R. P. (2020). Evaluation of the non-perturbed TEC reference of a new version of the DIX. Brazilian Journal of Geophysics, 38(3), 1–10. https://doi.org/10.22564/rbgf.v38i3.2056

Picanço, G. A. S., Denardini, C. M., Nogueira, P. A. B., Barbosa-Neto, P. F., Resende, L. C. A., Chen, S. S., Carmo, C. S., Moro, J., Romero-Hernandez, E., & Silva, R. P. (2021). Equatorial ionospheric response to storm-time electric fields during two intense geomagnetic storms over the Brazilian region using a Disturbance Ionosphere indeX. Journal of Atmospheric and Solar–Terrestrial Physics, 223, e105734. https://doi.org/10.1016/j.jastp.2021.105734

Picanço, G. A. S., Denardini, C. M., Nogueira, P. A. B., Resende, L. C. A., Carmo, C. S., Chen, S. S., Barbosa-Neto, P. F., & Romero-Hernandez, E. (2022). Study of the equatorial and low-latitude total electron content response to plasma bubbles during solar cycle 24–25 over the Brazilian region using a Disturbance Ionosphere indeX. Annales Geophysicae, 40, 503–517. https://doi.org/10.5194/angeo-40-503-2022

Pimenta, A., Bittencourt, J., Fagundes, P., Sahai, Y., Buriti, R., Takahashi, H., & Taylor, M. J. (2003). Ionospheric plasma bubble zonal drifts over the tropical region: A study using OI 630nm emission all-sky images. Journal of Atmospheric and Solar-Terrestrial Physics, 65(10), 1117–1126. https://doi.org/10.1016/S1364-6826Resende, L. C. A.; Denardini, C. M.; Picanço, G. A. S.; Moro, J.; Barros, D.; Figueiredo, C. A. O. B.; Silva, R. P. On developing a new ionospheric plasma index for Brazilian equatorial F region irregularities, Annales Geophysicae, v. 37, p. 807–818, 2019. https://doi.org/10.5194/angeo-37-807-2019.

Santos, A. M., Abdu, M. A., Sobral, J. H. A., Mascarenhas, M., & Nogueira, P. A. B. (2013). Equatorial evening prereversal vertical drift dependence on solar EUV flux and F10.7 index during quiet and disturbed periods over Brazil. Journal of Geophysical Research: Space Physics, 118, 4662–4671. https://doi.org/10.1002/jgra.50438

Singh, S., Bamgboye, D. K., Mcclure, J. P., & Johnson, F. S. (1997). Morphology of equatorial plasma bubbles. Journal of Geophysical Research, 102(A9), 20019-20029. https://doi.org/10.1029/97JA01724

Takahashi, H., Wrasse, C., Denardini, C., Pádua, M., PAULA, E., Costa, S., Otsuka, Y., Shiokawa, K., Monico, J., Ivo, A., & Sant'anna, N. (2016). Ionospheric TEC weather map over South America. Space Weather, 14, 937-949. https://doi.org/10.1002/2016SW001474

Takahashi, H., Wrasse, C. M., Figueiredo, C. A. O. B., Barros, D., Abdu, M. A., Otsuka, Y., & Shiokawa, K. (2018). Equatorial plasma bubble seeding by MSTIDs in the ionosphere. Progress in Earth and Planetary Science, 5(32). https://doi.org/10.1186/s40645-018-0189-2

Taori, A., Parihar, N., Ghodpage, R., Dashora, N., Sripathi, S., Kherani, E. A., & Patil, P. T. (2015). Probing the possible trigger mechanisms of an equatorial plasma bubble event based on multistation optical data. Journal of Geophysical Research, 120(10), 8835–8847. https://doi.org/10.1002/2015ja021541

Tsunoda, R. T. (1985). Control of the seasonal and longitudinal occurrence of equatorial scintillations by the longitudinal gradient in the integrated E region Pedersen conductivity. Journal of Geophysical Research: Space Physics, 90, 447-456. https://doi.org/10.1029/JA090iA01p00447

Wan, X., Xiong, C., Rodriguez-Zuluaga, J., Kervalishvili, G. N., Stolle, C., & Wang, H. (2018). Climatology of the occurrence rate and amplitudes of local time distinguished equatorial plasma depletions observed by Swarm satellite. Journal of Geophysical Research: Space Physics, 123, 3014–3026. https://doi.org/10.1002/2017JA025072.

Wen, D., & Mei, D. (2020). Ionospheric TEC disturbances over China during the strong geomagnetic storm in September 2017. Advances in Space Research, 65(11), 2529-2539. https://doi.org/10.1016/j.asr.2020.03.002

Wilken, V., Kriegel, M., Jakowski, N., & Berdermann, J. (2018). An ionospheric index suitable for estimating the degree of ionospheric perturbations. Journal of Space Weather and Space Climate, 8(A19). https://doi.org/10.1051/swsc/2018008

Whalen, J. A. (2002). Dependence of equatorial bubbles and bottomside spread on season, magnetic activity, and E-region drift velocity during solar maximum. Journal of Geophysical Research, 107(A2), 1024. https://doi.org/10.1029/2001JA000039

Woodman, R. F., & La Hoz, C. (1976). Radar observations of F region equatorial irregularities. Journal of Geophysical Research, 81(31), 5447–5466. https://doi.org/z0.1029/JA081i031p05447

Wrasse, C. M., Figueiredo, C. A. O. B., Barros, D., Takahashi, H., Carrasco, A. J., Vital, L. F. R., Rezende, L. C. A., Egito, F., Rosa, G. M., & Sampaio, A. H. R. (2021). Interaction between Equatorial Plasma Bubbles and a Medium-Scale Traveling Ionospheric Disturbance, observed by OI 630 nm airglow imaging at Bom Jesus de Lapa, Brazil. Earth and Planetary Physics, 5(5), 397–406. https://doi.org/10.26464/epp2021045